ImmunoPET/NIRF/Cerenkov multimodality imaging of ICAM-1 in pancreatic ductal adenocarcinoma

Miao Li[#1,2], **Weijun Wei**[#2,3], **Todd E. Barnhart**[4], **Dawei Jiang**[2], **Tianye Cao**[2], **Kevin Fan**[2], **Jonathan W. Engle**[4], **Jianjun Liu**[3], **Weiyu Chen**[2], **Weibo Cai**[2,4]

[1]Department of Radiology, the First Affiliated Hospital of Xi'an Jiaotong University, 277 West Yanta Rd, Xi'an 710061, Shaanxi, China

[2]Department of Radiology, University of Wisconsin-Madison, Room 7137, 1111 Highland Ave, Madison, WI 53705, USA

[3]Department of Nuclear Medicine, Renji Hospital, School of Medicine, Shanghai Jiao Tong University, 1630 Dongfang Rd, Shanghai 200127, China

[4]Department of Medical Physics, University of Wisconsin-Madison, Room B1143, 1111 Highland Ave, Madison, WI 53705, USA

[#] These authors contributed equally to this work.

Abstract

Purpose—We dual-labeled an intercellular adhesion molecule-1 (ICAM-1) monoclonal antibody (mAb) and evaluated its effectiveness for lesion detection and surgical navigation in pancreatic ductal adenocarcinoma (PDAC) via multiple noninvasive imaging approaches, including positron emission tomography (PET), near-infrared fluorescence (NIRF), and Cerenkov luminescence imaging (CLI).

Methods—ICAM-1 expression in PDAC cell lines (BxPC-3 and AsPC-1) was assessed via flow cytometry and immunofluorescent staining. An ICAM-1 mAb labeled by IRDye 800CW and radionuclide zirconium-89 (denoted as [^{89}Zr]Zr-DFO-ICAM-1-IR800) was synthesized. Its performance was validated via in vivo comparative PET/NIRF/CLI and biodistribution (Bio-D) studies in nude mice bearing subcutaneous BxPC-3/AsPC-1 tumors or orthotopic BxPC-3 tumor models using nonspecific IgG as an isotype control tracer.

Results—ICAM-1 expression was strong in the BxPC-3 and minimal in the AsPC-1 cell line. Both multimodality imaging and Bio-D data exhibited more prominent uptake of [^{89}Zr]Zr-DFO-ICAM-1-IR800 in BxPC-3 tumors than in AsPC-1 tumors. The uptake of [^{89}Zr]Zr-DFO-IgG-IR800 in BxPC-3 tumors was similar to that of [^{89}Zr]Zr-DFO-ICAM-1-IR800 in AsPC-1 tumors.

These results demonstrate the desirable affinity and specificity of [^{89}Zr]Zr-DFO-ICAM-1-IR800 compared to [^{89}Zr]Zr-DFO-IgG-IR800. Orthotopic BxPC-3 tumor foci could also be clearly delineated by [^{89}Zr]Zr-DFO-ICAM-1-IR800. An intermodal match was achieved in the ICAM-1-targeted immunoPET/NIRF/CLI. The positive expression levels of ICAM-1 in BxPC-3 tumor tissue were further confirmed by immunohistopathology.

Conclusion—We successfully developed a dual-labeled ICAM-1-targeted tracer for PET/NIRF/CLI of PDAC that can facilitate better diagnosis and intervention of PDAC upon clinical translation.

Keywords

ImmunoPET; Near-infrared fluorescence (NIRF); Cerenkov luminescence imaging (CLI); Intercellular adhesion molecule-1 (ICAM-1); Pancreatic ductal adenocarcinoma (PDAC)

Introduction

Pancreatic ductal adenocarcinoma (PDAC) accounts for the majority of pancreatic cancers and is the fourth most lethal cancer type in the United States (US) [1]. Following diagnosis, the median survival time of PDAC patients is less than 6 months with a five-year survival rate of only 5%. The prognosis of PDAC would be improved if early diagnosis and intervention at the asymptomatic stage could be achieved. Currently, surgery is the only possible curative treatment for PDAC patients. However, only 15–20% of PDAC patients are suitable for surgery due to the presence of metastases at diagnosis. Even with surgical application, not all pancreatic cancer lesions can be resected. In addition, the misdiagnosis and understaging of PDAC can also interfere with the enrollment of patients for clinical trials [2]. As the final options, chemo- or radiotherapy are always modestly effective for advanced diseases but are associated with severe side effects. Therefore, there is an urgent demand for early and precise detection of PDAC [3].

The test of serum biomarkers can aid in the diagnosis of PDAC. For instance, carbohydrate antigen 19–9 (CA19–9) is a highly expressed tumor antigen approved by the US Food and Drug Administration (FDA) as a secreted biomarker for detecting PDAC [4, 5]. However, serum biomarkers are not ideal in terms of sensitivity and specificity and are unable to locate specific tumor lesions [5]. Another biomarker, intercellular adhesion molecule-1 (ICAM-1), was also proposed as a serum biomarker for the differentiation of PDAC and pancreatitis [6, 7]. Moreover, the upregulated expression of ICAM-1 in PDAC tissue has been verified by many studies [8–12], demonstrating that ICAM-1 may serve as a valuable biomarker for PDAC imaging.

In addition to serum testing, presurgical visualization for accurate lesion identification would improve patient stratification, anatomical orientation, and radical resection. Currently, morphologic imaging techniques, such as ultrasonography, endoscopy, computed tomography (CT), and magnetic resonance imaging (MRI), have been applied to the diagnosis of PDAC. However, these techniques are insensitive to subtle biological alterations, even with assistance from contrast agents [2]. In addition to aforementioned modalities, positron emission tomography (PET) is the only option of functional imaging

modality for the clinical diagnosis of PDAC [13], possessing advantages in sensitivity, selectivity, and quantification [12]. However, it is often difficult for the most popular PET tracer, i.e., [18F]fluoro-deoxy-glucose (FDG), to distinguish between malignant and benign pancreatic conditions, which result results in the inevitable false positivity. [18F]fluoro-deoxy-*L*-thy-midine (FLT) has also been utilized for evaluating the cell proliferation in PDAC, but its efficacy is suboptimal due to the relatively high uptake in liver. Given the mutual enhancement between hypoxia and desmoplasia existing in PDAC tissue, some nitroimidazole-derived tracers, such as [18F]fluoro-misonidazole (FMISO) and [18F]fluoro-azomycin-arabinoside (FAZA), are employed for the hypoxic imaging of PDAC. Unfortunately, the slow diffusion and low contrast within target tissue hinder their expansion in real applications [13]. To over-come these defects, antibody tracers are exploited for their avidity/specificity to limit interference from physiological uptake and enhance contrast between target/nontarget tissues. For clinical translation, a PET tracer developed from an FDA-approved monoclonal antibody (mAb) is preferred [14, 15].

Aside from presurgical diagnosis, targeted visualization of PDAC tissue can also provide an intraoperative navigation. However, CT, MRI, and PET cannot be operated conveniently on-site in surgical scenarios [16]. Optical imaging, specifically near-infrared fluorescence (NIRF, 700–900 nm) imaging, has become a feasible solution to solve this issue in recent years [17]. NIRF imaging has enhanced imaging resolution and tissue penetration compared to the most commonly used ultrasonography.

Compared to monochannel scanning for each modality, the combination of PET and NIRF/Cerenkov luminescence imaging (CLI) can offer increased resolution, sensitivity, tissue penetration, and quantification. This method integrates advantages of each modality and provides synergistic merits in both whole-body localization of lesions and accurate delineation of tumor margins. Based on a previous study [18], we attempted to devise a near-infrared fluorophore and positron emitter dual-labeled mAb as a platform to map the gross morphology of PDAC lesions. In our previous work, we developed a mAb-derived ICAM-1-targeted radiotracer [64Cu]Cu-NOTA-ICAM-1 and demonstrated the potency of [64Cu]Cu-NOTA-ICAM-1 immunoPET in effectively diagnosing melanomas and anaplastic thyroid cancers [19]. In the current study, the same ICAM-1 mAb was dually labeled with IR800 and zir-conium-89. The performance of the novel tracer (i.e., [89Zr]Zr-DFO-ICAM-1-IR800) was investigated in murine PDAC models, aiming to provide a solution for ICAM-1-targeted multimodal imaging of PDAC.

Materials and methods

Reagents and materials

A mouse anti-human ICAM-1 mAb (clone: R6–5-D6) was obtained from BioXCell, Inc. (Lebanon, NH). 1-(4-Isothiocyanatophenyl)-3-[6,17-dihydroxy-7,10,18,21-tetraoxo-27-(N-acetylhydroxylamino)-6,11,17,22-tetraazaheptaeicosine]thiourea (p-SCN-deferoxamine or DFO) was purchased from Macrocyclics, Inc. (Dallas, Texas). IRDye 800CW-N-hydroxysuccinimide ester dye (IR800-NHS) was purchased from LI-COR Biosciences, Inc. (Lincoln, Nebraska). Alexa Fluor 488-labeled goat anti-mouse antibody was obtained from BioLegend, Inc. (San Diego, California). Pharmingen rat antimouse CD31 antibody was

purchased from BD Bioscience, Inc. (San Diego, California). Cy3-labeled donkey antirat antibody was obtained from Jackson ImmunoResearch Laboratories, Inc. (West Grove, Pennsylvania). A nonspecific human IgG isotype control was purchased from Invitrogen, Inc. (Rockford, Illinois). PD-10 desalting columns were purchased from GE Healthcare (Piscataway, NJ). Ultrafilters (30 kDa threshold) and all other reagents were provided by Thermo Fisher Scientific (Fair Lawn, New Jersey).

Conjugation with deferoxamine and labeling with IR800 dye

Briefly, the [89Zr]Zr-DFO-ICAM-1-IR800 tracer was synthesized by bioconjugation and radiocoordination chemistry in sequence. The conjugation of ICAM-1 mAb and DFO followed the procedure in our previous publication [20]. The final volume of reaction mixture was 300 μL, and the molar ratio of DFO/mAb was 10:1. The resulting reaction system was oscillated at room temperature (RT) for 2 h. After purification using a PD-10 cartridge with $1 \times$ PBS as the mobile phase, the fractions of product DFO-ICAM-1 mAb were concentrated into 500 μL via ultrafiltration with a centrifuge at $13,000 \times g$. IR800-NHS (5 μg) was dissolved in anhydrous DMSO (10 μL) to prepare the stock solution. The IR800-NHS stock solution was then spiked into a mixture of DFO-ICAM-1 mAb solution (3 mg/mL, 50 μL) and PBS/carbonate buffer (300 μL). The molar ratio of DFO-ICAM-1 mAb to IR800-NHS was adjusted to be 1:2. The conjugation reaction proceeded at RT for 2 h with oscillation in darkness. This reaction system was then purified by a PD-10 cartridge. The fractions of product DFO-ICAM-1-IR800 were concentrated into 150 μL with an ultrafilter. The IR800/DFO-modified IgG isotype control (DFO-IgG-IR800) was synthesized according to the same procedure.

Production and quality control of radiotracers

The preparation of zirconium-89 was conducted on a PETtrace cyclotron (GE Healthcare, Milwaukee, Wisconsin) at the University of Wisconsin-Madison (UW-Madison) via the nuclear reaction of $^{89}Y(p,n)^{89}Zr$ following a reported procedure [20]. The final chemical species of zirconium-89 was in oxalate form.

The pH value of the [89Zr]Zr oxalate (33.3 MBq or 0.9 mCi) diluted in HEPES buffer (500 μL, 0.5 M, pH 7.0) was adjusted to 7.0–7.5 by adding Na_2CO_3 solution (1 M).DFO-ICAM-1-IR800 (100 μg/mCi) was then added into the mixture. The radiolabeling reacted at 37 °C for 1 h on a thermostatic shaker with oscillation (700 rpm). Then, the reaction mixture was purified via a PD-10 cartridge. Eventually, the [89Zr]Zr-DFO-ICAM-1-IR800 fractions were collected and sterilized by a filter (0.22 μm). IR800/89Zr-labeled IgG ([89Zr]Zr-DFO-IgG-IR800) was prepared in the same manner.

The radiochemical purity and integrity of the tracer were assessed by instant thin-layer chromatography (iTLC) using a radio scanner (Eckert & Ziegler Inc.) with iTLC-SG plates (Agilent Inc.) and sodium citrate solution for development. Analytical size exclusion chromatography (SEC) was performed using an Infinity 1260 chromatograph (Agilent Inc.) with a Superdex™ 75 Increase 5/15 GL column (5×153–158 mm^2, ~9 μm). Radiocounts and absorbance (280 nm) were detected with a Packard A-100 radio detector and an ultraviolet (UV) detector in tandem, respectively.

Cell culture

Two human PDAC cell lines (i.e., BxPC-3 and AsPC-1) were obtained from the American Type Culture Collection (ATCC; Manassas, Virginia). The cells were propagated in Roswell Park Memorial Institute (RPMI)-1640 medium (high glucose; Gibco by Life Technologies, Inc.; Grand Island, New York) supplemented with 10% fetal bovine serum (FBS; Gemini Bioproducts, Inc.; West Sacramento, California) and incubated at 37 °C in a humidified constant-temperature incubator with 5% CO_2. When reached ~80% confluence, the cells were harvested for flow cytometry, immunofluorescence staining, or tumor inoculation.

Flow cytometry and immunofluorescence confocal imaging

The ICAM-1 expression profile in the BxPC-3 and AsPC-1 cell lines was tested by flow cytometry and immunofluorescent staining with imaging. For flow cytometry, the cells suspended in cold flow buffer (~1×10^7 cells/mL) were split into aliquots (~1.5×10^6 cells/tube). After blocking, the cells were incubated with cold $1 \times PBS$ (as blank control), goat antimouse antibody (as the controls of secondary antibody only; 5 μg/mL), and ICAM-1 mAb (as primary antibodies; 5 or 10 μg/mL) for 1 h in an ice bath. The cells stained with ICAM-1 mAb were washed with cold $1 \times PBS$ and then incubated with the goat anti-mouse antibody (5 μg/mL) for 1 h in an ice bath and darkness. All the samples stained with the secondary antibody were washed with cold $1 \times PBS$. Finally, cells in each sample were resuspended in cold $1 \times PBS$ (300 μL) and assayed on a 5-Laser LSR Fortessa cytometer (Becton-Dickinson, Inc.; San Jose, California). The data were analyzed using FlowJo software (ver. X.0.7; Tree Star, Inc.; Ashland, Oregon).

For immunofluorescent confocal imaging, cells were cultured in glass bottom dishes (Φ 50 mm, ~2×10^5 cells/dish) and propagated at 37 °C in CO_2 (5%) overnight. After blocking, cells were incubated with ICAM-1 mAb (as primary antibody; 10 μg/mL) at RT for 45 min followed by goat antimouse secondary antibody (5 μg/mL) at RT for 45 min in darkness. Cells were then stained with Hoechst 33342 (5 μg/mL; Life Technologies of Thermo Fisher; Eugene, Oregon) at RT for 30 min in darkness and imaged on an A1R confocal microscope (Nikon, Inc.; Melville, New York).

Mouse xenograft models

All the procedures of animal study were in compliance with regulations made by the Institutional Animal Care and Use Committee (IACUC), UW-Madison, and all other author affiliations. All PDAC mouse models were established in female athymic nude mice aged 4–5 weeks (Envigo Inc.). Before implantation, the cultured cells resuspended in cold $1 \times PBS$ were mixed with Matrigel (Corning by Discovery Labware, Inc.; Bedford, Massachusetts) at a ratio of 1:1 (v/v) and precooled in ice.

The cell suspension was injected subcutaneously (~5×10^6 cells/mouse) to establish subcutaneous xenograft models. Tumors were utilized for in vivo studies once their diameter reached 5–10 mm.

The orthotopic xenograft models were set up via laparotomy. All surgical operations fulfilled the requirements of aseptic practice. After the mice were fully anesthetized via respiration in

the flow of oxygen (1 L/min) and isoflurane (2.5%), skin on the upper flank of abdomen was disinfected with iodine and 75% ethanol. Incisions (~10 mm) were made on the skin and smooth muscle. The pancreas was exposed by gently pinching and pulling the spleen adjacent. The cell suspension loaded in the cold insulin syringe was injected into the pancreas head (50 μL/shot). After a 10-s pause, the needle was rotated and withdrawn slowly. Then, all the organs were returned to the peritoneal cavity by a Q-tip, and incisions on the muscle and skin layers were sutured. Antibiotic ointment and ketoprofen (5 mg/kg for subcutaneous injection) were administered for wound disinfection and pain relief. Tumor growth was monitored via palpation and ultrasonic imaging weekly, starting from the fourth week postinoculation. Tumors were ready for experimentation when the diameter reached ~5 mm [21–23].

PET/NIRF/CLI and biodistribution studies in subcutaneous models

In vivo multimodality imaging with [^{89}Zr]Zr-DFO-ICAM-1-IR800 or [^{89}Zr]Zr-DFO-IgG-IR800 (as a nonspecific isotype control) tracers was performed in sequence at preset time points postinjection (p.i.). An Inveon Micro-PET/CT scanner (Siemens Medical Solutions USA, Inc.) was employed for PET imaging. Mice bearing PDAC tumors were administered 5–10 MBq (0.14–0.27 mCi) of [^{89}Zr]Zr-DFO-ICAM-1-IR800 or [^{89}Zr]Zr-DFO-IgG-IR800 via lateral tail vein injection and were placed in a prone posture on the scanner bed. The original imaging data were acquired by running the micro-PET/CT scanner for 5–15 min in static mode without attenuation or scatter correction. The PET images were reconstructed by the three-dimensional ordered subset expectation maximization (OSEM3D) algorithm with regions of interest (ROIs) drawn manually using Inveon Research Workshop (IRW) software (Siemens, Inc.). The quantification of ROI uptake in major organs was used to calculate the percent of injected dose per gram (%ID/g) by dividing the tissue activity in MBq/g by the total radioactivity of injection (with decay correction). Once PET scanning was accomplished, the mice were immediately moved to the IVIS Spectrum imaging system (PerkinElmer, Inc.; Waltham, Massachusetts) for NIRF/CLI acquisition. The wavelengths of NIRF excitation/emission were 745 nm and 800 nm, respectively. The fluorescent radiant efficiency of tumors was quantified on Advanced Acquisition and Analysis Tools software (PerkinElmer, Inc.) via manual delineation of tumor ROI. The exposure time of CLI acquisition was 120 s.

Immediately after imaging at 120 h p.i., all mice were sacrificed and dissected. Blood, major organs, and tumors were collected and weighed immediately. The radiocounts of each sample were assayed on a Wizard 2480 automatic γ-counter (PerkinElmer, Inc.) and converted into %ID/g with decay correction.

PET/NIRF imaging, biodistribution and in situ NIRF/CLI studies in orthotopic models

PET/NIRF imaging of orthotopic models was performed using the same parameters as the imaging of subcutaneous models. The orthotopic mouse models were placed in a lateral posture during all optical imaging steps for better exposure of lesion signals. A radioactive biodistribution (Bio-D) study was conducted following optical imaging using the same procedure as previously described.

For the in situ ex vivo NIRF/CLI, the mice administered [^{89}Zr]Zr-DFO-ICAM-1-IR800 were euthanized during the point of peak uptake within the tumor as indicated by PET/NIRF ROI kinetics. Photos of the intact body were first taken under white light. The abdominal cavity of the mice was then opened on the left flank with orthotopic tumors exposed. NIRF/CLI was performed before and after the resection of orthotopic tumors.

Immunohistology

Tumor blocks were frozen immediately after resection and cut into slices (5 μm in thickness) in the Experimental Pathology Laboratory at the Carbone Cancer Center, UW-Madison. Briefly, tumor sections were fixed in cold acetone for 10 min and dried in air for 3 min at RT. After blocking for 30 min at RT, sections were incubated with the ICAM-1 mAb (as primary antibody; 10 μg/mL) overnight at 4 °C and then incubated with goat antimouse antibody (as secondary antibody; 5 μg/mL) for 1 h at RT. Adjacent sections from the same tumor were also stained with rat antimouse CD31 (vascular endothelium biomarker) antibody (as the primary antibody; 10 μg/mL) overnight at 4 °C followed by donkey antirat antibody (as secondary antibody; 5 μg/mL) for 1 h at RT. After infiltration with Vectashield medium containing 4′,6-diamidino-2-phenylindole (DAPI; Vector Laboratories, Inc.; Burlingame, California), the tissue sections were sealed with coverslips. All fluorescent images were acquired on an A1R confocal microscope (Nikon, Inc.; Melville, New York).

Statistical analysis

Quantitative data are presented as the mean ± standard deviation (SD). Statistical tests of mean uptake values were under-taken using Student's t test. $p < 0.05$ was considered statistically significant.

Results

Differential ICAM-1 expression in PDAC cell lines

As shown in the flow cytometry chart (Fig. 1a), increased ICAM-1 expression was observed in BxPC-3 cells but not in AsPC-1 cells. The immunofluorescent staining of ICAM-1 in the same cell lines further confirmed strong signals in the BxPC-3 cells (Fig. 1b). These in vitro results showed that the BxPC-3 cell line is suitable for developing ICAM-1-positive tumor models, whereas the AsPC-1 tumor model serves as a negative control.

Production, characterization and quality control of [^{89}Zr]Zr-DFO-ICAM-1-IR800

According to the reported methodology regarding ^{89}Zr/NIRF dye dual-labeling of mAb, the self-quenching of IR800 would be induced when the distance of two molecules was less than 10 nm, which is the typical diameter of a mAb molecule [24, 25]. Therefore, we chose a validated mAb-to-dye molar ratio (1:2) for the conjugation reaction. The bifunctional chelator DFO was linked to the ICAM-1 mAb using the classical amine-isothiocyanate reaction, whereas the IR800 dye was incorporated into the resulting mAb by the conventional amine-NHS-ester reaction. After the final purification with a PD-10 column, the specific activity achieved was approximately 9.8 ± 1.4 mCi/mg (362.6.9 ± 51.8 MBq/mg) for all the antibody tracers ($n = 6$). The nondecay-corrected radiochemical yield of all ^{89}Zr-labeling reactions was greater than 70%. The radiochemical purity of [^{89}Zr]Zr-

DFO-ICAM-1-IR800 is >99% (Fig. S1b), and the molecular integrity of tracer is acceptable (> 97%; Fig. S1c, S1d; both indicated by peak area normalization), and it remained stable in $1 \times$ PBS within 3 h after purification (Fig. S1b).

PET/NIRF imaging and biodistribution studies in subcutaneous PDAC models

In comparison, the performance of PET/NIRF imaging strategy was examined in three groups of subcutaneous tumor models: (1) mice bearing BxPC-3 tumors administered [^{89}Zr]Zr-DFO-ICAM-1-IR800 ($n = 4$); (2) mice bearing AsPC-1 tumors administered [^{89}Zr]Zr-DFO-ICAM-1-IR800 ($n = 5$); and (3) mice bearing BxPC-3 tumors injected with nonspecific [^{89}Zr]Zr-DFO-IgG-IR800 ($n = 5$). Based on the ROI analysis shown in Fig. 2a, the deposition of [^{89}Zr]Zr-DFO-ICAM-1-IR800 in subcutaneous BxPC-3 tumors is evident at the earliest time point (4 h p.i.). It reaches a peak ($9.8 \pm 2.7\%$ID/g) at 24 h p.i. and then declines gradually over time. The uptake curve of [^{89}Zr]Zr-DFO-ICAM-1-IR800 in the subcutaneous AsPC-1 tumors (Fig. 2b) grew initially and gradually reached a plateau (3.1 ± 0.6–$4.2 \pm 0.4\%$ID/g) at 48 h p.i. The signal of [^{89}Zr]Zr-DFO-IgG-IR800 in the subcutaneous BxPC-3 tumors (Fig. 2c) increased slightly after injection with a peak uptake of $5.0 \pm 1.2\%$ID/g ($n = 5$) and decreased slowly from 24 h p.i. to the end of scanning ($3.6 \pm 0.9\%$ID/g). The tumor uptake of tracers in the two control groups (the latter two aforementioned groups) was equal to the background level. The kinetic plots of other major organs exhibited similar patterns among all three groups with subcutaneous tumors, depicting the typical action of radiolabeled antibodies. When compared with the area under the curve (AUC) of blood pool uptake between Groups 1 and 2 (Fig. 2a and b), there was a statistically significant difference ($p < 0.05$), which may result from the lack of a tumor "sink" effect or the potential presence of a circulating antigen that could interact with [^{89}Zr]Zr-DFO-ICAM-1-IR800 in the BxPC-3 models. Moreover, the maximum intensity projection (MIP) images exhibited a visible contrast of tumor mass between Group 1 (Fig. 2e) and Group 2 (Fig. 2f). The same can be seen in the MIP between Group 1 (Fig. 2e) and Group 3 (Fig. 2g). A clear discrepancy among three groups in terms of qualitative tumor uptake was noted at 24 h p.i. (Fig. 2; $p < 0.05$). The series of representative MIP images covering all time points are provided in Fig. S2. A proportion of [^{89}Zr]Zr-DFO-ICAM-1-IR800 was catabolized in the liver, and the degradants may be excreted from the hepatobiliary system. These in vivo results validate the good avidity and specificity of [^{89}Zr]Zr-DFO-ICAM-1-IR800.

The ex vivo Bio-D assay was conducted at 120 h p.i. (Fig. 3). Among all three groups (Groups 1–3), the PET ROI and Bio-D exhibited a similar tracer distribution at 120 h p.i. (Table S1, S2). Figure 3 shows that the radioactivity difference of tumors in Group 1 compared to the two control groups (Groups 2 and 3) was obvious (9.2 ± 2.3 vs 4.9 ± 1.3, $p < 0.05$; 9.2 ± 2.3 vs $4.1 \pm 1.2\%$ ID/g, $p < 0.05$; Table S2), highlighting the superior specificity of [^{89}Zr]Zr-DFO-ICAM-1-IR800. Almost all nontargeted tissues displayed minimal signals, except for the liver and spleen. For liver uptake at 120 h p.i., the value extracted from the PET ROI appears to be greater than the value from the Bio-D assay, which may relate to the process of ROI-drawing and scatter reconstruction corrections. Taken together, the PET uptake data correlated well with the Bio-D data and reflected the tumor-targeting ability of the ICAM-1-targeted tracer in vivo.

The in vivo NIRF images were also acquired from three groups of subcutaneous tumor models (Groups 1–3) in the same timeframe. The kinetics of the tumor-to-muscle ratio (TMR) were calculated on the ROI data to prevent interference from surrounding tissue (Fig. 4). The peak of TMR in Group 1 was at 24 h p.i. Among all groups, TMR kinetics exhibited a similar trend compared to those with the above time-radioactivity curves (Fig. 2). This reflects the consistency in PET/NIRF imaging and excellent stability of the dual-labeled tracers in vivo. The TMR in Group 1 was considerably greater than that in Groups 2 ($p < 0.05$) or 3 ($p < 0.05$) (Fig. 4, Table S3), which also confirms the excellent specificity of [^{89}Zr]Zr-DFO-ICAM-1-IR800. As shown in Fig. S3, the tumor contrast between Group 1 and Group 2 (or Group 3) was remarkable in terms of NIRF fluorescence.

PET/NIRF imaging and biodistribution studies in orthotopic PDAC models

Furthermore, the PET/NIRF imaging modalities were evaluated between subcutaneous BxPC-3 (i.e., Group 1 in the previous section) and orthotopic BxPC-3 tumor model administered [^{89}Zr]Zr-DFO-ICAM-1-IR800 (Group 4; $n = 3$). The peak uptake of radiotracers within tumors occurred at 24 h p.i. in both groups (Fig. 2a, d and Table S1). In the coronal, sagittal, and transversal PET images, a sharp delineation of orthotopic BxPC-3 tumors against background tissues was present (Fig. 2h, i, and j).

In the Bio-D study, the radioactive accumulation in Group 4 validated the ROI quantitative results (Fig. 3). The results from tumors in Groups 3 and 4 were similar (9.2 ± 2.3 vs $7.6 \pm 1.5\%$ ID/g, Fig. 3, Table S2).

As the orthotopic BxPC-3 tumor underwent the process of becoming superficial under the pushing of abdominal organs, the position of tumors could be further confirmed by palpation. The difference in TMR between Groups 1 and 4 was insignificant ($p > 0.05$, Fig. 4, Table S3). However, outlines of orthotopic BxPC-3 tumors and the adjacent spleen could be well distinguished on the PET images (Fig. 2h, i and j). These results indicate the consistency and reproducibility of PET/NIRF imaging in diagnosing BxPC-3 tumors (both subcutaneous and orthotopic models).

Image-guided resection of orthotopic PDACs

To test the feasibility of [^{89}Zr]Zr-DFO-ICAM-1-IR800 tracers in guiding surgeries, we performed in situ ex vivo optical imaging in white light, NIRF, and CLI modalities. As depicted in Fig. 5, the position and contour of orthotopic BxPC-3 tumors after laparotomy matched perfectly among the three modalities. Orthotopic BxPC-3 tumor nodules were successfully removed via simulative resection, which was well presented by relocation of the sharp signal. Colocalization by PET/NIRF/CLI enables accurate surgery navigation that facilitates negative surgical margins. These results demonstrate the effectiveness of [^{89}Zr]Zr-DFO-ICAM-1-IR800 tracer in visualizing PDAC and guiding subsequent total resection of tumor tissues.

Immunofluorescent staining and imaging studies

Finally, histopathological studies were performed to characterize the ICAM-1 distribution within tumor tissues. The confocal images of tumor tissues exhibited intense ICAM-1 and

CD31 staining in BxPC-3 tumor tissues but not in malignant tissues of AsPC-1 (Fig. 6). The green ICAM-1 signal overlayed the periphery of tumor cells, which is similar to that were detected in the in vitro immunofluorescent staining studies (Fig. 1b). No obvious overlay between ICAM-1 and nuclei (DAPI) or neovasculature (CD31) was observed. In comparison, ICAM-1 expression in subcutaneous BxPC-3 tumors was spotted, whereas a much lower signal was detected within AsPC-1 tumors. These results further confirm that the in vivo expression of ICAM-1 in BxPC-3 tumors correlates well with the PET/NIRF imaging and Bio-D results above.

Discussion

Classical targets for imaging PDAC include integrin $\alpha_v\beta_6$, carcinoembryonic antigen (CEA), and CA19–9, among others [12, 13, 26, 27]. To the best of our knowledge, ICAM-1 has not been tested as an imaging target for PDAC to date. ICAM-1 is a representative member of the transmembrane glycoprotein belonging to the immunoglobulin superfamily of cell adhesion molecules (CAMs) that plays an important role in inflammation, immune response, tumor progression, and metastasis. ICAM-1-targeted imaging may pave a way for visualizing cell-cell/cell-matrix adhesion processes [28]. The physiological expression of ICAM-1 on fibroblasts, endothelial cells, and some leukocytes is minimal, but the expression can be enhanced by cytokines. The upregulated level of ICAM-1 in PDAC tissue has been verified repeatedly [8–12]. ICAM-1 could be shed into the blood circulation to generate soluble ICAM-1 (sICAM-1), which serves as a reliable serum biomarker for PDAC [2]. ICAM-1 is also a promising target in PDAC therapy [29], so the design of an ICAM-1-targeted theranostic pair for PDACs is expected in future studies. In our case, the contrast between tumor and background tissue was not remarkable when compared to results obtained by a dually labeled CA19–9-specific agent [18]. Relatively low expression of ICAM-1 and sICAM-1 in the circulation, different antibody and fluorophore properties, and different conjugation strategies (random vs site-specific) are potential reasons accounting for discordance.

In addition to PET, Raman optics, ultrasonography, MRI, and single-photon emission computed tomography were also utilized in the targeted imaging of ICAM-1. However, their sensitivity and quantitative potency are less satisfactory [30–34]. In the dual-labeling scenarios of mapping pancreatic cancer, NIRF was employed as a general optical modality [18, 35–37]. In addition, ICAM-1 has been implemented for NIRF imaging of breast cancer and atherosclerosis [34, 38]. In this study, we presumed and validated the value of NIRF as a secondary modality for imaging PDAC. Several studies have reported multimodal imaging of PDAC [18, 35–37]. Specifically, the merits of dual-modal PET/NIRF imaging include precise localization of tumor lesions, guidance during endoscopy/biopsy, and determination of positive tumor margins during surgical resection [26]. Dual labeling of the same mAb molecule allows for a thorough evaluation of PDAC on two identical signal sources. In addition, the development and use of dual-labeled tracers are more cost-effective than the corresponding monofunctional agents.

As depicted in Fig. 2 and Fig. 4, the kinetics of tumor uptake revealed a similar trend within the same combination of tracers and models during the same imaging period. The

contrasting signals from [^{89}Zr]Zr-DFO-ICAM-1-IR800 between BxPC-3 and AsPC-1 tumors and between the dual-labeled ICAM-1 mAb and IgG within BxPC-3 tumors reached a peak at 24 h p.i. (Fig. 4). These results validate the excellent correlation between NIRF and PET imaging and demonstrate the specificity of ICAM-1-targeted imaging strategy developed in this work. Nevertheless, the in vivo quantification of NIRF radiant efficiency is not accurate enough due to the attenuation of fluorescence caused by surface tissues during transmission. Therefore, NIRF quantification may only be suitable for superficial lesions or in the scenario of endoscopy/intraoperative visualization. The intense physiological uptake of radiolabeled antibodies in the liver and spleen can be efficiently blocked/saturated by pre/coinjection of unlabeled antibody, as shown by a recent study [39].

After the confirmation of the in vivo avidity and specificity of [^{89}Zr]Zr-DFO-ICAM-1-IR800 in subcutaneous tumor models, we further assessed this tracer in an orthotopic BxPC-3 xenograft model to mimic a surgical resection scene. The tumor was deeply seated in the pancreas head, but it was still squeezed aside by adjacent organs (Fig. 2h, i, j) and became palpable through muscle/skin layers due to the soft texture and slim shape of the pancreas. Superficial positioning minimized the attenuation of NIRF from the tumors and facilitated in vivo NIRF imaging. The optical contrast between pre- and postresection orthotopic xenografts was sharp, as expected, despite the unavoidable autofluorescence or background signal from the surrounding tissues (Fig. 5).

Similar to CA19–9 [39], the dissemination of sICAM-1 might capture and consume a small portion of [^{89}Zr]Zr-DFO-ICAM-1-IR800, compromising the tumor-targeting potency of the agent. In our case, an escalated dose of [^{89}Zr]Zr-DFO-ICAM-1-IR800 was administered to compensate for such consumption. As a result, both subcutaneous and orthotopic PDACs could be delineated by [^{89}Zr]Zr-DFO-ICAM-1-IR800 immunoPET imaging. For the existence of sICAM-1, high concentrations may affect clearance and targeting. Even if the ratio of blood CA19–9 concentration between pancreatic cancer subjects and healthy controls (~10) is considerably increased compared with the same ratio of sICAM-1 (~1.6) [40]; the imaging performance of a similarly dual-labeled antibody tracer toward CA19–9 was not seriously impaired [18], indicating that interference from serum ligands may not be a significant concern. Regardless, serum ICAM-1 analysis is still highly recommended before in vivo targeted imaging of ICAM-1, which can assist with the stratification of PDAC patients who will benefit from imaging [28]. Furthermore, the impact of sICAM-1 on the distribution and tumor-targeting ability of immunoPET probes needs to be investigated in future studies. The moderate uptake within the spleen may be partially ascribed to the tracer self-aggregation that was caused by the concentrated hydrophobic IR800 dye moiety [18, 39, 41]. The higher uptake seen within the spleen of the orthotopic BxPC-3 model compared to the subcutaneous model may be attributed to the inflammation caused by the orthotopic implantation of BxPC-3 tumors.

In this study, we used a mouse antihuman ICAM-1 mAb, which did not reflect the physiological expression of murine ICAM-1 molecules. Using genetically engineered animal models expressing human ICAM-1 and fully human or humanized ICAM-1 mAb may better replicate the interaction between tracers and their targets. For clinical translation, we developed nanobodies by immunization of alpacas with human ICAM-1. Our ongoing

studies are investigating the theranostic value of nanobody-based ICAM-1-targeted agents in various human malignancies, including PDACs.

Conclusion

In summary, we reported that ICAM-1 is a viable biomarker for PDAC and that ICAM-1-targeted PET/NIRF/CLI of PDAC is feasible in preclinical settings. Optimized ICAM-1-targeted imaging may facilitate better management of PDAC in terms of patient screening, image-guided surgery, and treatment response assessment.

Supplementary Material

Refer to Web version on PubMed Central for supplementary material.

Acknowledgements

References

1. Siegel RL, Miller KD, Jemal A. Cancer statistics, 2020. CA Cancer J Clin. 2020;70(1):7–30. 10.3322/caac.21590. [PubMed: 31912902]

2. Laeseke PF, Chen R, Jeffrey RB, Brentnall TA, Willmann JK. Combining in vitro diagnostics with in vivo imaging for earlier detection of pancreatic ductal adenocarcinoma: challenges and solutions. Radiology. 2015;277(3):644–61. 10.1148/radiol.2015141020. [PubMed: 26599925]

3. Singhi AD, Koay EJ, Chari ST, Maitra A. Early detection of pancreatic cancer: opportunities and challenges. Gastroenterology. 2019;156(7):2024–40. 10.1053/j.gastro.2019.01.259. [PubMed: 30721664]

4. Resovi A, Bani MR, Porcu L, Anastasia A, Minoli L, Allavena P, et al. Soluble stroma-related biomarkers of pancreatic cancer. Embo Mol Med. 2018;10(8):e8741. 10.15252/emmm.201708741. [PubMed: 29941541]

5. Loosen SH, Neumann UP, Trautwein C, Roderburg C, Luedde T. Current and future biomarkers for pancreatic adenocarcinoma. Tumor Biol. 2017;39(6):1010428317692231. 10.1177/1010428317692231.

6. Jenkinson C, Elliott V, Menon U, Apostolidou S, Fourkala OE, Gentry-Maharaj A, et al. Evaluation in pre-diagnosis samples discounts ICAM-1 and TIMP-1 as biomarkers for earlier diagnosis of pancreatic cancer. J Proteome. 2015;113:400–2. 10.1016/j.jprot.2014.10.001.

7. Mohamed A, Saad Y, Saleh D, Elawady R, Eletreby R, Kharalla AS, et al. Can serum ICAM 1 distinguish pancreatic cancer from chronic pancreatitis? Asian Pac J Cancer Prev. 2016;17(10):4671–5. 10.22034/APJCP.2016.17.10.4671. [PubMed: 27892682]

8. Schwaeble W, Kerlin M, Meyerzum Büschenfelde K, Dippold W. De novo expression of intercellular adhesion molecule 1(ICAM-1, CD54) in pancreas cancer. Int J Cancer. 1993;53(2):328–33. 10.1002/ijc.2910530226. [PubMed: 8093883]

9. Shimoyama S, Gansauge F, Gansauge S, Widmaier U, Oohara T, Beger HG. Overexpression of intercellular adhesion molecule-1 (ICAM-1) in pancreatic adenocarcinoma in comparison with normal pancreas. Pancreas. 1997;14(2):181–6. 10.1097/00006676-199703000-00011. [PubMed: 9057191]

10. Tempia-Caliera AA, Horvath LZ, Zimmermann A, Tihanyi TT, Korc M, Friess H, et al. Adhesion molecules in human pancreatic cancer. J Surg Oncol. 2002;79(2):93–100. 10.1002/jso.10053. [PubMed: 11815996]

11. Hayes SH, Seigel GM. Immunoreactivity of ICAM-1 in human tumors, metastases and normal tissues. Int J Clin Exp Pathol. 2009;2(6):553–60. [PubMed: 19636402]

12. Tummers WS, Willmann JK, Bonsing BA, Vahrmeijer AL, Gambhir SS, Swijnenburg RJ. Advances in diagnostic and intraoperative molecular imaging of pancreatic cancer. Pancreas. 2018;47(6):675–89. 10.1097/MPA.0000000000001075. [PubMed: 29894417]

13. Cornelissen B, Knight JC, Mukherjee S, Evangelista L, Xavier C, Caobelli F, et al. Translational molecular imaging in exocrine pancreatic cancer. Eur J Nucl Med Mol Imaging. 2018;45(13):2442–55. 10.1007/s00259-018-4146-5. [PubMed: 30225616]

14. England CG, Hernandez R, Eddine SBZ, Cai W. Molecular imaging of pancreatic cancer with antibodies. Mol Pharm. 2016;13(1):8–24. 10.1021/acs.molpharmaceut.5b00626. [PubMed: 26620581]

15. King J, Bouvet M, Singh G, Williams J. Improving theranostics in pancreatic cancer. J Surg Oncol. 2017;116(1):104–13. 10.1002/jso.24625. [PubMed: 28513912]

16. Zhang Y, Hong H, Engle JW, Yang Y, Theuer CP, Barnhart TE, et al. Positron emission tomography and optical imaging of tumor CD105 expression with a dual-labeled monoclonal antibody. Mol Pharm. 2012;9(3):645–53. 10.1021/mp200592m. [PubMed: 22292418]

17. Zhang Y, Hong H, Severin GW, Engle JW, Yang Y, Goel S, et al. ImmunoPET and near-infrared fluorescence imaging of CD105 expression using a monoclonal antibody dual-labeled with 89Zr and IRDye 800CW. Am J Transl Res. 2012;4(3):333–46. [PubMed: 22937210]

18. Houghton JL, Zeglis BM, Abdel-Atti D, Aggeler R, Sawada R, Agnew BJ, et al. Site-specifically labeled CA19.9-targeted immunoconjugates for the PET, NIRF, and multimodal PET/NIRF imaging of pancreatic cancer. Proc Natl Acad Sci U S A. 2015;112(52):15850. 10.1073/pnas.1506542112. [PubMed: 26668398]

19. Wei W, Jiang D, Lee HJ, Li M, Kutyreff CJ, Engle JW, et al. Development and characterization of CD54-targeted immunoPET imaging in solid tumors. Eur J Nucl Med Mol Imaging. 2020. 10.1007/s00259-020-04784-0.

20. Li M, Jiang D, Barnhart TE, Cao T, Engle JW, Chen W, et al. Immuno-PET imaging of VEGFR-2 expression in prostate cancer with 89Zr-labeled ramucirumab. Am J Cancer Res. 2019;9(9): 2037–46. [PubMed: 31598404]

21. Kim MP, Evans DB, Wang H, Abbruzzese JL, Fleming JB, Gallick GE. Generation of orthotopic and heterotopic human pancreatic cancer xenografts in immunodeficient mice. Nat Protoc. 2009;4: 1670–80. 10.1038/nprot.2009.171. [PubMed: 19876027]

22. Dai L, Lu C, Long XY, Dai J, Zhou JX. Construction of orthotopic xenograft mouse models for human pancreatic cancer. Exp Ther Med. 2015;10:1033–8. 10.3892/etm.2015.2642. [PubMed: 26622435]

23. Moreno JA, Sanchez A, Hoffman RM, Nur S, Lambros MP. Fluorescent orthotopic mouse model of pancreatic cancer. J Vis Exp. 2016;115:e54337. 10.3791/54337.

24. Hong H, Zhang Y, Severin GW, Yang Y, Engle JW, Niu G, et al. Multimodality imaging of breast cancer experimental lung metastasis with bioluminescence and a monoclonal antibody dual-labeled with 89Zr and IRDye 800CW. Mol Pharm. 2012;9(8):2339–49. 10.1021/mp300277f. [PubMed: 22784250]

25. Hernandez R, Sun H, England CG, Valdovinos HF, Ehlerding EB, Barnhart TE, et al. CD146-targeted immunoPET and NIRF imaging of hepatocellular carcinoma with a dual-labeled monoclonal antibody. Theranostics. 2016;6(11):1918–33. 10.7150/thno.15568. [PubMed: 27570560]

26. Dimastromatteo J, Brentnall T, Kelly KA. Imaging in pancreatic disease. Nat Rev Gastroenterol Hepatol. 2017;14(2):97–109. 10.1038/nrgastro.2016.144. [PubMed: 27826137]

27. de Geus SWL, Boogerd LSF, Swijnenburg R, Mieog JSD, Tummers WSFJ, Prevoo HAJM, et al. Selecting tumor-specific molecular targets in pancreatic adenocarcinoma: paving the way for image-guided pancreatic surgery. Mol Imaging Biol. 2016;18(6):807–19. 10.1007/s11307-016-0959-4. [PubMed: 27130234]

28. Boonstra MC, De Geus SWL, Prevoo HAJM, Hawinkels LJAC, Van De Velde CJH, Kuppen PJK, et al. Selecting targets for tumor imaging: an overview of cancer-associated membrane proteins. Biomark Cancer. 2016;8:119–33. 10.4137/BIC.S38542. [PubMed: 27721658]

29. Brooks KJ, Coleman EJ, Vitetta ES. The antitumor activity of an anti-CD54 antibody in SCID mice xenografted with human breast, prostate, non-small cell lung, and pancreatic tumor cell lines. Int J Cancer. 2008;123(10):2438–45. 10.1002/ijc.23793. [PubMed: 18752248]

30. Deddens LH, van Tilborg GAF, van der Marel K, Hunt H, van der Toorn A, Viergever MA, et al. In vivo molecular MRI of ICAM-1 expression on endothelium and leukocytes from subacute to chronic stages after experimental stroke. Transl Stroke Res. 2017;8(5):440–8. 10.1007/s12975-017-0536-4.

31. Noonan J, Asiala SM, Grassia G, Macritchie N, Gracie K, Carson J, et al. In vivo multiplex molecular imaging of vascular inflammation using surface-enhanced Raman spectroscopy. Theranostics. 2018;8(22):6195–209. 10.7150/thno.28665. [PubMed: 30613292]

32. Yan F, Sun Y, Mao Y, Wu M, Deng Z, Li S, et al. Ultrasound molecular imaging of atherosclerosis for early diagnosis and therapeutic evaluation through leucocyte-like multiple targeted microbubbles. Theranostics. 2018;8(7):1879–91. 10.7150/thno.22070. [PubMed: 29556362]

33. Mosley M, Torres JB, Allen D, Cornelissen B. Immuno-imaging of ICAM-1 in tumours by SPECT. Nucl Med Biol. 2020;84–85:73–9. 10.1016/j.nucmedbio.2020.02.014.

34. Zhang Y, Wang M, Liu W, Peng X. Optical imaging of triple-negative breast cancer cells in xenograft athymic mice using an ICAM-1-targeting small-molecule probe. Mol Imaging Biol. 2019;21(5):835–41. 10.1007/s11307-018-01312-3. [PubMed: 30623283]

35. Luo H, England CG, Goel S, Graves SA, Ai F, Liu B, et al. ImmunoPET and near-infrared fluorescence imaging of pancreatic cancer with a dual-labeled bispecific antibody fragment. Mol Pharm. 2017;14(5):1646–55. 10.1021/acs.molpharmaceut.6b01123. [PubMed: 28292180]

36. Wang Q, Yan H, Jin Y, Wang Z, Huang W, Qiu J, et al. A novel plectin/integrin-targeted bispecific molecular probe for magnetic resonance/near-infrared imaging of pancreatic cancer. Biomaterials. 2018;183:173–84. 10.1016/j.biomaterials.2018.08.048. [PubMed: 30172243]

37. Zettlitz KA, Tsai WK, Knowles SM, Kobayashi N, Donahue TR, Reiter RE, et al. Dual-modality immuno-PET and near-infrared fluorescence imaging of pancreatic cancer using an anti-prostate stem cell antigen Cys-diabody. J Nucl Med. 2018;59(9):1398–405. 10.2967/jnumed.117.207332. [PubMed: 29602820]

38. Bertrand M, Abran M, Maafi F, Busseuil D, Merlet N, Mihalache-Avram T, et al. In vivo near-infrared fluorescence imaging of atherosclerosis using local delivery of novel targeted molecular probes. Sci Rep. 2019;9(1):2670. 10.1038/s41598-019-38970-4. [PubMed: 30804367]

39. Lohrmann C, O'Reilly EM, O'Donoghue JA, Pandit-Taskar N, Carrasquillo JA, Lyashchenko SK, et al. Retooling a blood-based biomarker: phase I assessment of the high-affinity CA19–9 antibody HuMab-5B1 for immuno-PET imaging of pancreatic cancer. Clin Cancer Res. 2019;25(23):7014–23. 10.1158/1078-0432.CCR-18-3667. [PubMed: 31540979]

40. Faca VM, Song KS, Wang H, Zhang Q, Krasnoselsky AL, Newcomb LF, et al. A mouse to human search for plasma proteome changes associated with pancreatic tumor development. PLoS Med. 2008;5(6):e123. 10.1371/journal.pmed.0050123. [PubMed: 18547137]

41. Sharma SK, Chow A, Monette S, Vivier D, Pourat J, Edwards KJ, et al. Fc-mediated anomalous biodistribution of therapeutic antibodies in immunodeficient mouse models. Cancer Res. 2018;78(7):1820–32. 10.1158/0008-5472.CAN-17-1958. [PubMed: 29363548]

a

b

Scale bar: 100 μm
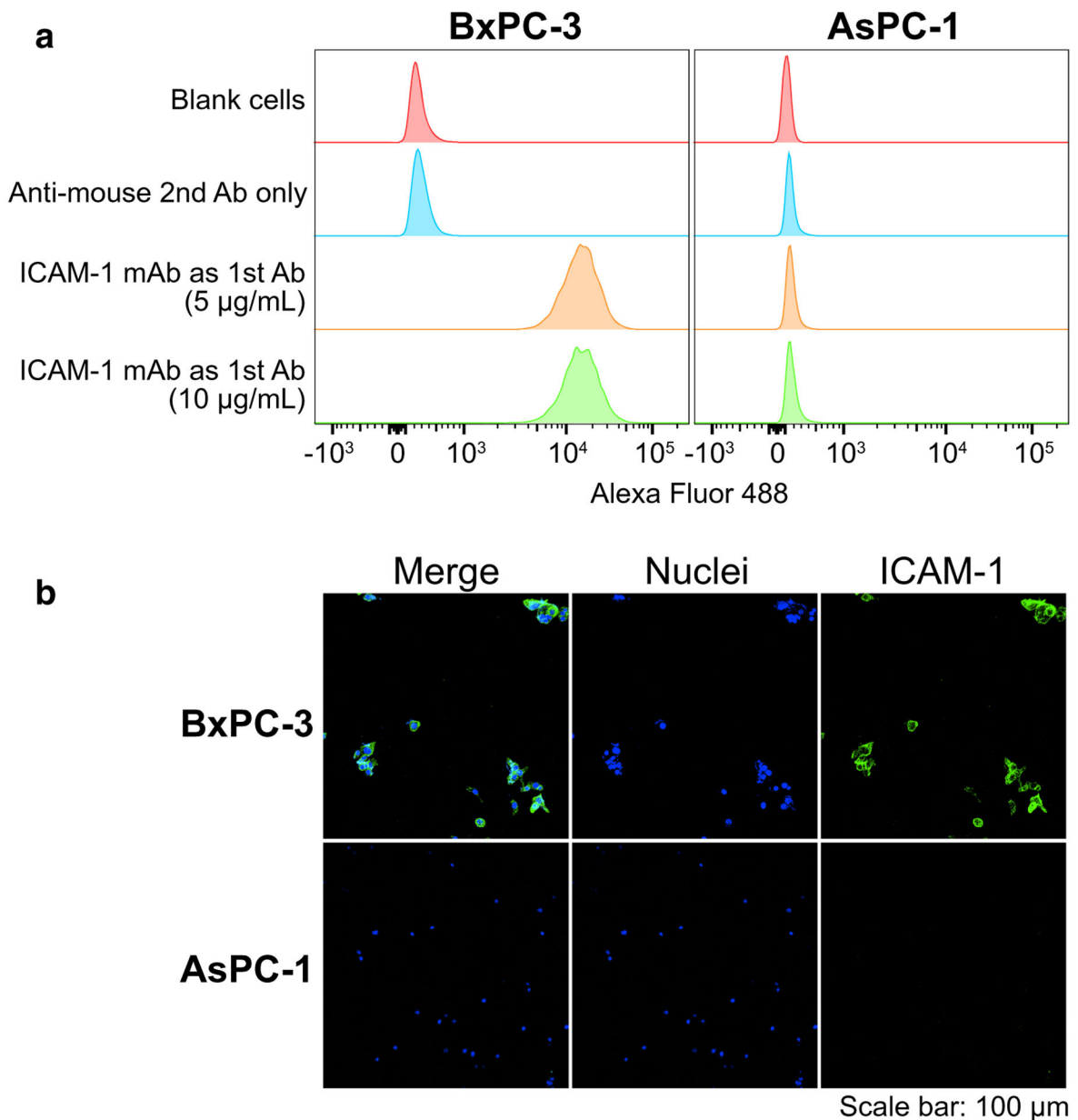
Fig. 1.
In vitro ICAM-1 expression in pancreatic ductal adenocarcinoma (PDAC) cell lines (BxPC-3 and AsPC-1) confocal imaging after immunofluorescent staining. Panels: **a** flow cytometry ($n = 3$); **b** confocal imaging after immunofluorescent staining. Sample groups: the controls were engaging with goat anti-mouse secondary antibody only (anti-mouse 2nd Ab only); the samples were engaging with mouse anti-human ICAM-1 monoclonal antibody as the primary stain (ICAM-1 mAb as 1st Ab); the cell nuclei stained by Hoechst (Nuclei); the samples were engaging with mouse anti-human ICAM-1 monoclonal antibody as the primary stain (ICAM-1)
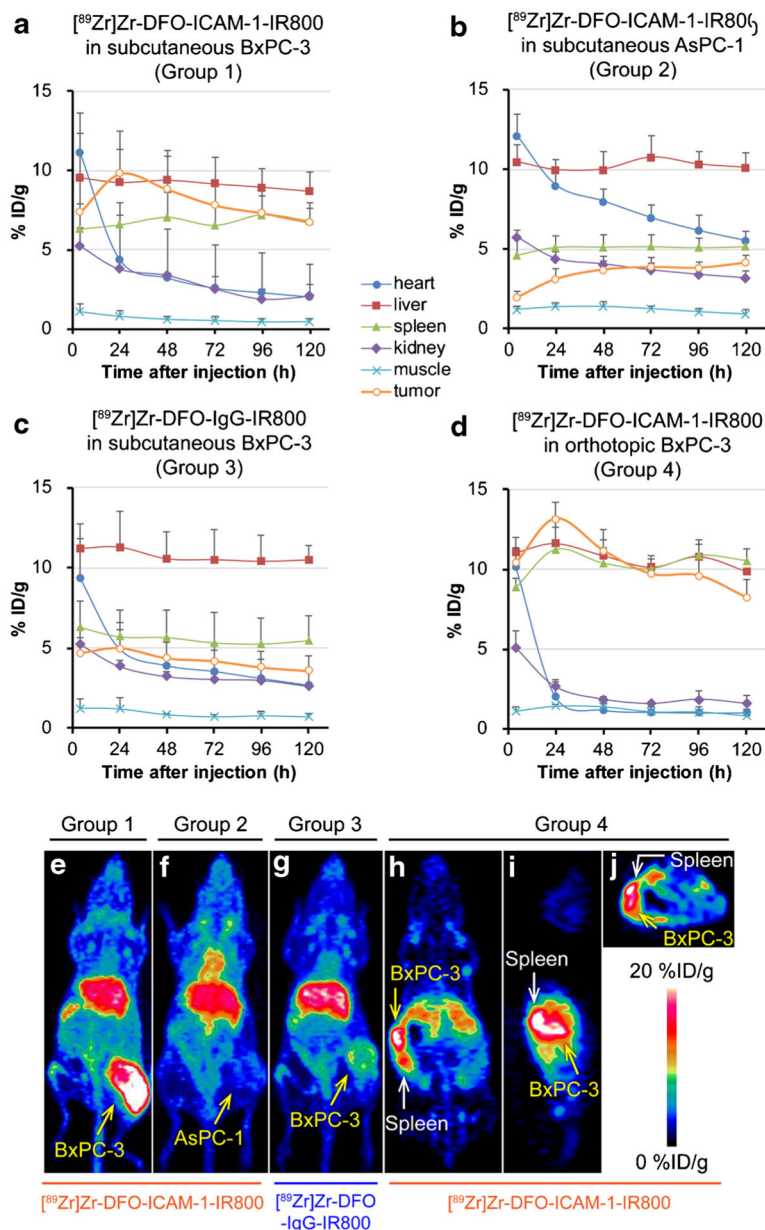
Fig. 2.

The uptake kinetics of region of interest (ROI) and typical maximum intensity projections (MIP) and tomograms at 24 h post-injection (p.i.) in the in vivo positron emission tomography (PET) images of nude mice bearing subcutaneous and orthotopic pancreatic ductal adenocarcinoma (PDAC) tumors (BxPC-3 and AsPC-1). $p < 0.05$. Panels: **a** IR800/[89]Zr dual-labeled ICAM-1 monoclonal antibody ([89Zr]Zr-DFO-ICAM-1-IR800) injected into subcutaneous BxPC-3 models (Group 1; $n = 4$); **b** [89Zr]Zr-DFO-ICAM-1-IR800 injected into subcutaneous AsPC-1 models (Group 2; $n = 5$); **c** IR800/[89]Zr dual-labeled IgG isotype control ([89Zr]Zr-DFO-IgG-IR800) injected into subcutaneous BxPC-3 models (Group 3; n = 5); **d** [89Zr]Zr-DFO-ICAM-1-IR800 injected into orthotopic BxPC-3 models (Group 4; $n = 3$); **e** MIP of subcutaneous BxPC-3 models injected with [89Zr]Zr-

DFO-ICAM-1-IR800 (Group 1); **f** MIP of subcutaneous AsPC-1 models injected with [^{89}Zr]Zr-DFO-ICAM-1-IR800 (Group 2); **g** MIP of subcutaneous BxPC-3 models injected with [^{89}Zr]Zr-DFO-IgG-IR800 (Group 3); coronal (**h**), sagittal (**i**), and transverse (**j**) sections of orthotopic BxPC-3 models injected with [^{89}Zr]Zr-DFO-ICAM-1-IR800 (Group 4)
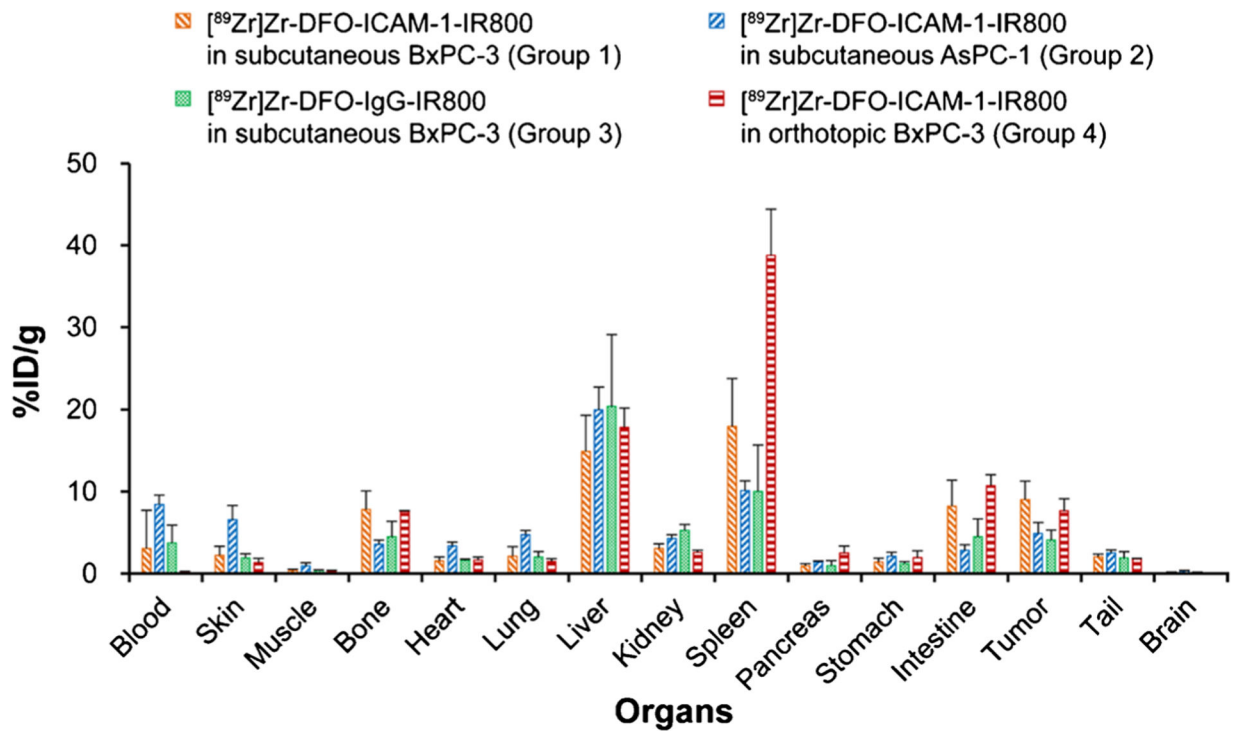
Fig. 3.
The radioactive biodistribution (Bio-D) of IR800/^{89}Zr dual-labeled ICAM-1 monoclonal antibody ([^{89}Zr]Zr-DFO-ICAM-1-IR800) or IgG control ([^{89}Zr]Zr-DFO-IgG-IR800) in the tumors and major organs of subcutaneous or orthotopic pancreatic ductal adenocarcinoma (PDAC) models (BxPC-3 and AsPC-1). $p < 0.05$. Groups: IR800/^{89}Zr dual-labeled ICAM-1 monoclonal antibody ([^{89}Zr]Zr-DFO-ICAM-1-IR800) injected into subcutaneous BxPC-3 models (Group 1; $n = 4$); [^{89}Zr]Zr-DFO-ICAM-1-IR800 injected into subcutaneous AsPC-1 models (Group 2; $n = 5$); IR800/^{89}Zr dual-labeled IgG isotype control ([^{89}Zr]Zr-DFO-IgG-IR800) injected into subcutaneous BxPC-3 models (Group 3; $n = 5$); [^{89}Zr]Zr-DFO-ICAM-1-IR800 injected into orthotopic BxPC-3 models (Group 4; $n = 3$)
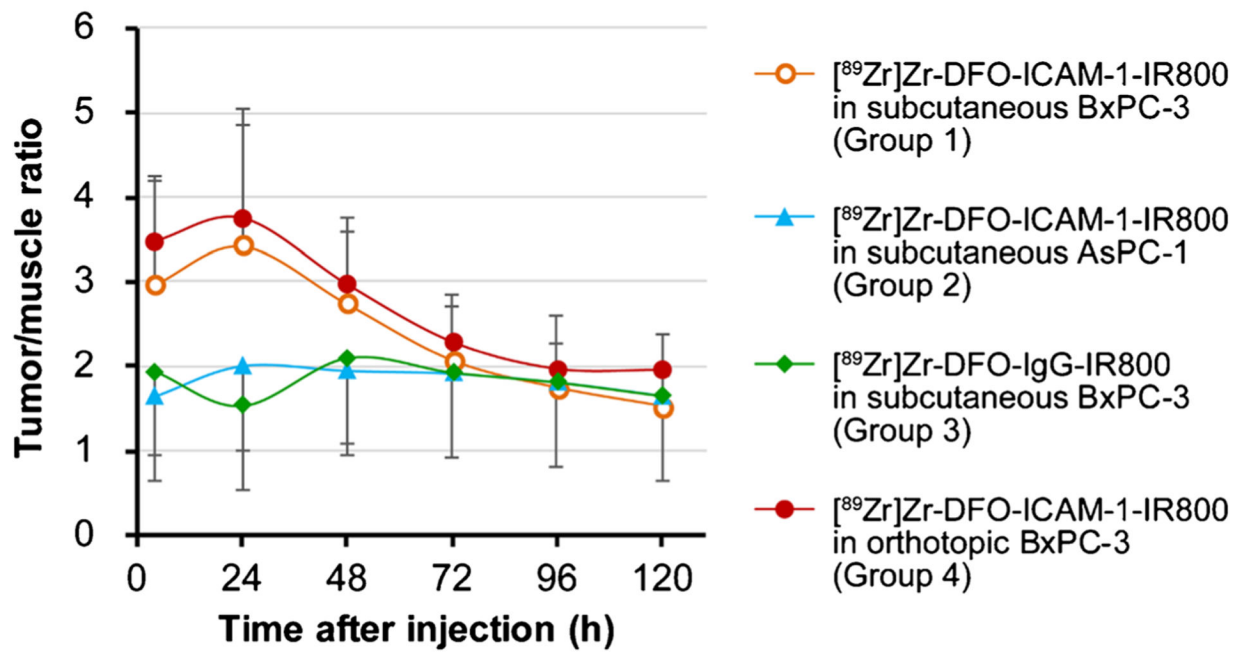
Fig. 4.

The kinetics of tumor-to-muscle ratio (TMR) of average radiant efficiency withdrawn from the region of interest (ROI) in the in vivo near-infrared fluorescent (NIRF) images of nude mice bearing subcutaneous and orthotopic PDAC tumors (BxPC-3 and AsPC-1). $p < 0.05$. Groups: IR800/^{89}Zr dual-labeled ICAM-1 monoclonal antibody ([^{89}Zr]Zr-DFO-ICAM-1-IR800) injected into subcutaneous BxPC-3 models (Group 1; $n = 4$); [^{89}Zr]Zr-DFO-ICAM-1-IR800 injected into subcutaneous AsPC-1 models (Group 2; $n = 5$); IR800/^{89}Zr dual-labeled IgG control ([^{89}Zr]Zr-DFO-IgG-IR800) injected into subcutaneous BxPC-3 models (Group 3; $n = 5$); [^{89}Zr]Zr-DFO-ICAM-1-IR800 injected into orthotopic BxPC-3 models (Group 4; $n = 3$)
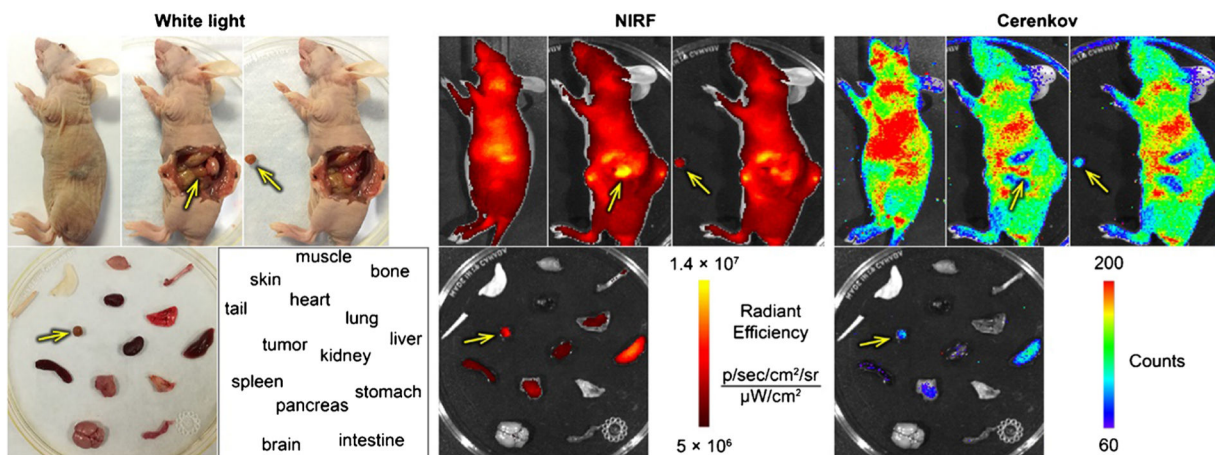
Fig. 5.

The in situ ex vivo optical imaging of typical nude mice bearing orthotopic BxPC-3 tumor at 120 h post-injection (p.i.) for the simulation of tumor resection surgery. NIRF, near-infrared fluorescence. Arrows: BxPC-3 tumor. The position and contour of the orthotopic BxPC-3 tumor match perfectly between modalities of white light, NIRF, and Cerenkov luminescence imaging (CLI) after laparotomy. The removal of the orthotopic BxPC-3 tumor is well presented by the relocation of the signal from the original tumor site to the resected nodule
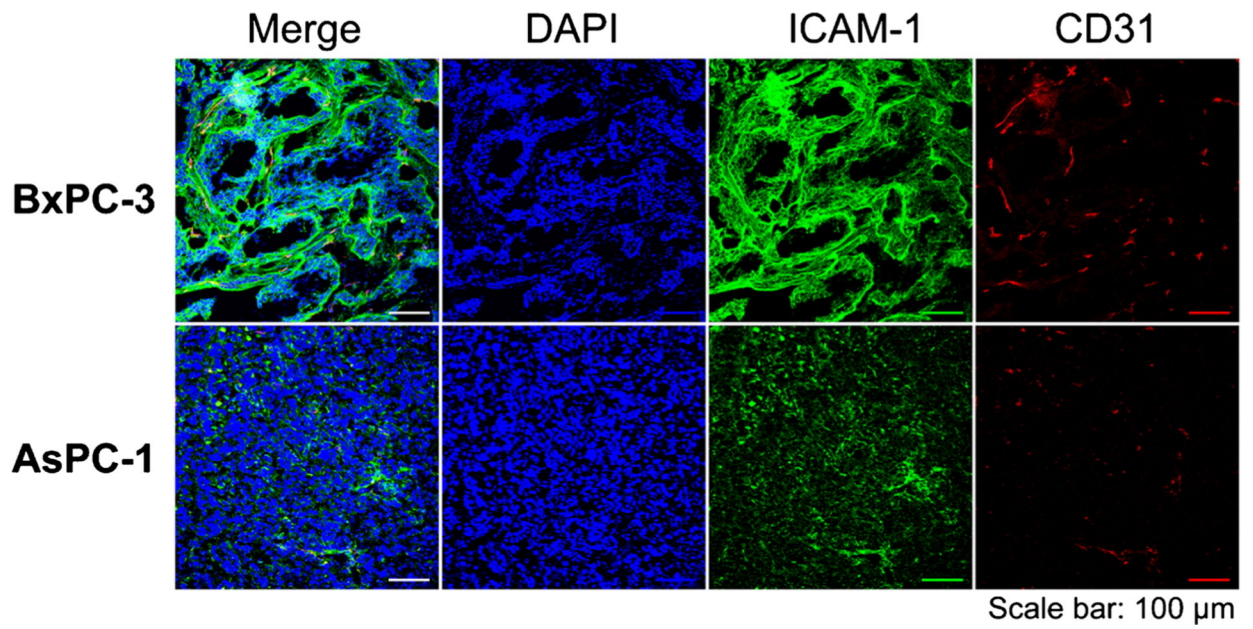
Fig. 6.

The confocal imaging of tissues from the subcutaneous pancreatic ductal adenocarcinoma (PDAC) tumors after immunofluorescent staining. Sample groups: DAPI, cell nucleus stained by DAPI; ICAM-1, the expression of ICAM-1 stained by ICAM-1 monoclonal antibody as the primary stain; CD31, the expression of vascular endothelium biomarker CD31